Eddy genesis and manipulation
in plane laminar shear flow

M. Scholle, A. Haas, N. Aksel

Department of Applied Mechanics and Fluid Dynamics,

University of Bayreuth, D–95440 Bayreuth, Germany

and

M.C.T. Wilson, H.M. Thompson, P.H. Gaskell

School of Mechanical Engineering, University of Leeds,

Leeds, LS2 9JT, UK

Abstract

Eddy formation and presence in a plane laminar shear flow configuration consisting of two infinitely long plates orientated parallel to each other is investigated theoretically. The upper plate, which is planar, drives the flow; the lower one has a sinusoidal profile and is fixed. The governing equations are solved via a full finite element formulation for the general case and semi-analytically at the Stokes flow limit. The effects of varying geometry (involving changes in the mean plate separation or the amplitude and wavelength of the lower plate) and inertia are explored separately. For Stokes flow and varying geometry, excellent agreement between the two methods of solution is found. Of particular interest with regard to the flow structure is the importance of the clearance that exists between the upper plate and the tops of the corrugations forming the lower one. When the clearance is large, an eddy is only present at sufficiently large amplitudes or small wavelengths.

1

However, as the plate clearance is reduced, a critical value is found which triggers the formation of an eddy in an otherwise fully attached flow for any finite amplitude and arbitrarily large wavelength. This is a precursor to the primary eddy to be expected in the lid-driven cavity flow which is formed in the limit of zero clearance between the plates. The influence of the flow driving mechanism is assessed by comparison with corresponding solutions for the case of gravity-driven fluid films flowing over an undulating substrate. When inertia is present, the flow generally becomes asymmetrical. However, it is found that for large mean plate separations the flow local to the lower plate becomes effectively decoupled from the inertia dominated overlying flow if the wavelength of the lower plate is sufficiently small. In such cases the local flow retains its symmetry. A local Reynolds number based on the wavelength is shown to be useful in characterising these large-gap flows. As the mean plate separation is reduced, the form of the asymmetry caused by inertia changes, and becomes strongly dependent on the plate separation. For lower plate wavelengths which do not exhibit a kinematically induced secondary eddy, an inertially induced secondary eddy can be created if the mean plate separation is sufficiently small and the global Reynolds number sufficiently large.

1 Introduction

The problem of laminar shear flow in a fluid confined between two rigid surfaces, one fixed the other moving, remains one of fundamental interest, with Couette flow between two infinite, perfectly parallel flat plates being arguably the archetypal example; another is Taylor-Couette flow in the small gap formed between two concentrically aligned cylinders. Not surprisingly, the literature associated with these two classical problems is correspondingly vast, but an overview of their essential features can be found in, for example, Tritton [1], Spurk & Aksel [2].

In practice, the confining rigid surfaces generating a shear flow are rarely everywhere completely equidistant from each other. This might be by design or due to eccentricity inherent

within the system, as in the case of fluid film lubrication [3]. The surfaces involved may also feature additional complicating factors in the form of random surface asperities or well-defined surface patterning, which can occur either naturally or as a consequence or indeed requirement of a particular manufacturing process [4]. Manufactured functional surfaces arise across a broad swathe of engineering applications and have particular relevance with respect to lubricant friction problems [5], where regular surface patterning is being used increasingly to improve the performance of tribological components [6]. The key feature that unifies these and related problems is that, even in the absence of inertia, irregular confining geometry is a trigger for eddy formation [7].

The presence of eddies is of both practical and scientific interest since the onset of recirculating flow can enhance load carrying capacity significantly and reduce frictional drag in, for example, lubricated contacts [8, 9], as well as affecting wear characteristics by trapping loose, sub-micron particles [6]. Related examples of where exploration of the effects of local flow structure within laminar shear flow has proved extremely informative include the role played by eddies in industrial roll coaters [10, 11, 12], eddy formation and the effect of localised disturbances on stagnation lines [13, 14], and eddy motions and flow patterns [15, 16, 17]. Eddies have also been shown recently to play an important role in enhancing mass transport [18], and global heat transfer via thermal mixing [19].

The focus of the present investigation is that of laminar shear flow between two horizontally aligned plates; the driving upper plate being planar, the lower one fixed and having a sinusoidal profile. Of particular relevance is the early work of Pozrikidis [20] for the case of creeping flow in two-dimensional periodic channels, which he formulated using a boundary integral method for Stokes flow. This work provided detailed streamline plots of the underlying flow structure and established a criterion for flow reversal; results that remained at the forefront for almost two decades before influencing subsequent complementary theoretical investigations. The first of these was for the case of Stokes flow through a wavy walled channel [21, 22], followed recently by the case of Couette flow for the same problem, including non-zero Reynolds number effects in the context of the onset of flow separation [23]. Exploration of the latter was, however, limited by the analytical approach adopted. What remains

outstanding and forms the thrust of the present work is a systematic exploration to identify those factors which govern/control the size, shape and presence of eddies as the confining geometry (mean plate separation, or amplitude and wavelength of the lower plate) is varied — not just in the creeping flow limit but when significant inertia effects are present also, in order to reveal and understand the subtle inter-play between the two.

The problem under consideration is specified in Section 2, together with the two methods of solution employed. The first, and principal, method involves a full finite element solution of the Navier-Stokes and continuity equations; the second is comprised of a semi-analytical variational formulation for Stokes flow, solved using Ritz's direct method. This is followed, Section 3, by the results from a comprehensive and systematic investigation of the combined effects of changes to the flow geometry and inertia present on local flow structure; comparisons with corresponding gravity-driven free-surface film flow over an inclined wavy substrate [24], are drawn. Of particular interest is the kinematic and inertial manipulation of eddies. The findings are summarised in Section 4.

2   Problem Specification and Solution

2.1   Flow geometry, field equations and boundary conditions

The two-dimensional, steady, isothermal shear flow of an incompressible Newtonian liquid, of density ρ and constant dynamic viscosity η, confined between two horizontally aligned rigid plates is considered. The upper flat plate, moving with speed U_0, is separated by a mean distance H from the stationary lower one which has a sinusoidal profile. The solution domain and associated (X, Y) coordinate system are shown in Fig. 1, where $Y = 0$ corresponds to the mean position of the wavy lower plate. The governing steady Navier–Stokes and continuity equations for the velocity field $\boldsymbol{U} = (U, V)$ and the pressure P are, in dimensional form,

$$\rho \left(\boldsymbol{U} \cdot \nabla \right) \boldsymbol{U} \;\; = \;\; -\nabla P + \eta \nabla^2 \boldsymbol{U} \,, \tag{1}$$

$$\nabla \cdot \boldsymbol{U} \;\; = \;\; 0. \tag{2}$$
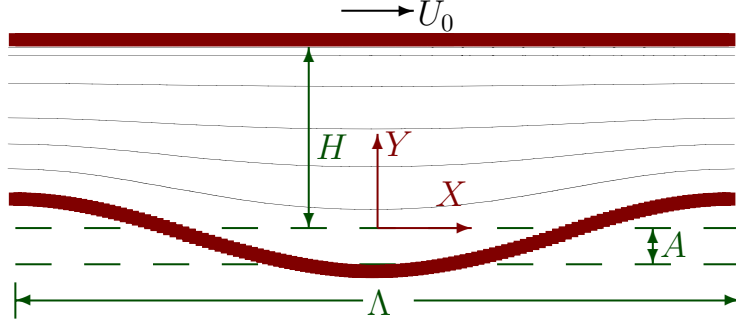
Figure 1: Schematic of the defining geometry for plane laminar shear flow between a flat moving upper and a fixed corrugated lower plate.

Along the lower plate, the profile of which is given by $B(X) = -A \cos (2\pi X/\Lambda)$, where A is the amplitude and Λ the wavelength, the fluid velocity satisfies the no–slip condition

$$\boldsymbol{U} (X, Y = B(X)) = \boldsymbol{0} \, , \tag{3}$$

while at the upper flat plate $Y = H$ the inhomogeneous no–slip condition

$$\boldsymbol{U} (X, H) = (U_0, 0) \, , \tag{4}$$

holds. The problem is closed by the prescription of periodic boundary conditions for $\boldsymbol{U}$ and P to the left and right in the flow direction.

2.2   Methods of solution

Two different approaches are employed to solve the governing equations subject to the prescribed boundary conditions. The first and main method involves a full numerical solution using a finite element (FE) decomposition of the domain of interest; the second, restricted to Stokes flow conditions, takes the form of a semi-analytic series solution.

The governing equations are written in dimensionless form, with all lengths scaled by H, velocities by U_0, and stresses by $\eta U_0/H$. This results in the following dimensionless Navier–Stokes and continuity equations,

$$\mathrm{Re}(\boldsymbol{u} \cdot \nabla)\boldsymbol{u} = -\nabla p + \nabla^2 \boldsymbol{u} \, , \tag{5}$$

$$\nabla \cdot \boldsymbol{u} = 0 \, , \tag{6}$$

5

where lowercase symbols are dimensionless variables corresponding to their uppercase equivalents, and $\mathrm{Re} = \rho U_0 H / \eta$ is the Reynolds number. The contour of the lower plate is given by $y = b(x) = -(a/h)\cos(hx)$, where $a = 2\pi A / \Lambda$ and $h = 2\pi H / \Lambda$. Then, the no–slip conditions at the lower plate read

$$\boldsymbol{u}\left(x, y = b(x)\right) = \boldsymbol{0}\,, \tag{7}$$

while at the upper plate

$$\boldsymbol{u}\left(x, y = 1\right) = (1, 0)\,. \tag{8}$$

2.2.1 Finite Element Formulation

The field equations (5, 6) are solved using the same Bubnov-Galerkin weighted residual finite element (FE) method used by Scholle et al. [24] to investigate the corresponding problem of gravity-driven film flow over a corrugated substrate. However, the formulation is somewhat simpler in the present case, as the rigid upper plate requires less sophisticated treatment than a free-surface [25]. Accordingly, only a brief summary of the key features is provided below.

The domain is tessellated into triangular Taylor-Hood 'V6/P3' elements, over each of which the velocity and pressure fields are represented by means of biquadratic and bilinear interpolation functions, respectively. The system of algebraic FE equations corresponding to the governing partial differential equations is obtained by substituting the elemental representations of $\boldsymbol{u}$ and p into weak forms of (5) and (6), with the interpolating functions for $\boldsymbol{u}$ and p as the weights. The result is a set of algebraic residual equations to be solved for the nodal velocities and pressures.

At the solid boundaries the no–slip condition is applied by dropping the momentum residuals there and inserting the known values of u and v explicitly into the FE equations. Periodic flow boundary conditions are imposed at the inlet and outlet by assigning the same freedom number to corresponding velocity and pressure freedoms on the two boundaries.

The global matrix of FE equations was solved by Newton iteration, with the Jacobian inverted using the Frontal Method. For the linear Stokes flow cases, the problem is solved after a single iteration; for non-zero Re typically 4 iterations were sufficient to reduce the L_2

6

norm of the residuals to below 10^{-8}. Grid independence of solutions was investigated using three different mesh levels, with grid independence achieved with a mesh containing 6450 elements and 13125 nodes. All reported solutions were obtained using this mesh structure.

Determination of Stationary Points and Streamlines

The results presented below use the position of the centre of each eddy as a means of characterising them, especially in studying asymmetry arising from inertial effects. The continuous, piecewise biquadratic representation of the velocity field makes the FE method well suited for calculating accurately the points within the domain where both velocity components vanish.

For efficiency, the eddy centres are identified in a two-stage process. First an element-by-element sweep through the mesh is made to determine the maximum and minimum values of u and v in each element, and, from these, whether or not an eddy centre lies within the element. For each element identified as containing such a point, Newton iteration is then used to solve the two simultaneous biquadratic velocity equations to obtain the coordinates of the eddy centre.

The streamfunction field, ψ, is also represented biquadratically within each V6/P3 element, with streamfunction freedoms at each of the six nodes. The latter are obtained by solving a weighted residual form of the following Poisson–type equation

$$\nabla^2\psi = \frac{\partial u}{\partial y} - \frac{\partial v}{\partial x}\,, \tag{9}$$

with ψ specified everywhere on the boundaries. The value $\psi = 0$ is taken along the lower plate, and the variation of ψ at the periodic boundary is found by integrating the horizontal component of velocity along the boundary. The uppermost value then gives the streamfunction value of the upper plate.

The reported eddy depths are obtained by calculating the vertical distance from the lower plate to the point where the dividing streamline, or separatrix, crosses the vertical centreline of the domain. This is readily obtained by considering the edge of each element that lies along the centreline and solving the quadratic equation $\psi = 0$ along the element edge.

2.2.2 Semi–analytical approach (Stokes flow)

The FE method described above has been shown to produce results in very good agreement with previously published experimental flow visualisation of free-surface flows. In the present problem there is a lack of experimental data with which to compare, however it is possible to confirm the FE predictions for Stokes flow using a semi-analytical approach as follows. The field equations (5, 6) can be obtained by variation of the integral

$$I = \iint_A \mathcal{L}\left(\partial_i u_j, \xi\right) \, \mathrm{d}x \, \mathrm{d}y \tag{10}$$

over the flow domain A, with the Lagrangian

$$\mathcal{L} = \mathcal{L}\left(\partial_i u_j, \xi\right) = \Phi\left(\partial_i u_j\right) + \xi \partial_i u_i \, , \tag{11}$$

where Φ denotes the dissipation function

$$\Phi\left(\partial_i u_j\right) = 2\left(\partial_x u\right)^2 + \left(\partial_y u + \partial_x v\right)^2 + 2\left(\partial_y v\right)^2 \, , \tag{12}$$

and ξ is a Lagrange multiplier which is introduced in order that the continuity equation forms a kinematical constraint. According to Millikan [26], variation with respect to the fields u, v and ξ leads to the Stokes equations and the continuity equation respectively, provided that the Lagrange multiplier ξ is related to the pressure and given by $\xi = -p/2$.

According to the no–slip conditions (7), (8), the variations δu and δv of the velocity field have to vanish at the boundary. For the pressure p, however, allowing for free variation at the boundary leads, according to Anthony [27], to the additional Neumann-type boundary condition

$$n_i \frac{\partial \mathcal{L}}{\partial\left(\partial_i \xi\right)} = \boldsymbol{n} \cdot \boldsymbol{u} = 0 \, . \tag{13}$$

Hence, the kinematic boundary conditions along the upper and the lower plates, which are the normal components of (7, 8), feature automatically in the variational formulation, whereas the respective tangential components at these two boundaries have to be prescribed explicitly and depend on the choice of test functions.

Motivated by the periodicity of the fields in the x–direction, it is convenient to express u, v and p as truncated Fourier series expansions

$$p(x, y) = \sum_{n=-N}^{N} P_n(y) \exp\left(\mathrm{i}nhx\right) \, , \qquad u_i(x, y) = \sum_{n=-N}^{N} U_{i,n}(y) \exp\left(\mathrm{i}nhx\right) \, , \tag{14}$$

8

with $N \in \mathbb{N}$, in order to perform the integration over x in (10). It has been shown [28], that the Fourier representation exists only for a weakly undulating lower plate, a limitation that can be overcome by applying a Padé approximation as used by Malevich et al. [22, 23], which although straightforward is a laborious procedure. An alternative to direct use of the divergent series (14) is obtained by means of the following coordinate transformation

$$R = hx \,, \qquad Q = \frac{y - b(x)}{1 - b(x)} \,. \tag{15}$$

which maps the flow domain of interest to the rectangular domain $[0, 2\pi] \times [0, 1]$ over which the corresponding Fourier expansions for u, v and p converge,

$$p(R, Q) = \sum_{n=-N}^{N} p_n(Q) \exp\left(\mathrm{i}nR\right), \qquad u_i(R, Q) = \sum_{n=-N}^{N} u_{i,n}(Q) \exp\left(\mathrm{i}nR\right) . \tag{16}$$

Prior use of this 'non–orthogonal' series representation has led to rapid convergence, see for example Scholle et al. [19], with the series truncated at $N = 4$. Furthermore, a simplified form of the no–slip conditions (7) at the lower plate results by virtue of the transformation (15).

Ritz's direct method is employed in order to obtain the necessary semi-analytic solutions, the technical details of which are provided in Appendix A.

3   Results and discussion

In order to quantify the effects of geometric and material parameters on the formation, shape and size of eddies within the domain, it is useful to define a set of measurables with which to represent the eddies. These are shown in Fig. 2, where D is the eddy depth measured along the vertical centreline from the lowest point on the lower plate to the separatrix, C_Y is the elevation of the eddy centre above the lowest point, and ΔX is the horizontal position of the eddy centre relative to the centreline. For Stokes flow conditions, symmetry dictates that the eddy centre always lies on the centreline, so ΔX gives a simple measure of asymmetry resulting from inertial effects. Similarly, the quantity ΔD is the change in eddy depth from the corresponding Stokes solution. Note that 'horizontal' and 'vertical' here refer respectively to the directions parallel to and perpendicular to the upper uniform rigid plate.

Though the formulation and solution of the dimensionless governing equations uses the mean plate separation, H, as the characteristic length, in the discussion of results below it is more convenient to use either the wavelength, Λ, or amplitude, A, of the lower plate as the length scale. Since both scales are used to illustrate different features, most results are presented with the relevant scale explicitly stated. However, it is useful to specify a dimensionless parameter which characterises the geometry of the sinusoidally profiled plate; this is defined here as the waviness, $a = 2\pi A/\Lambda$. A corresponding dimensionless mean gap is also defined as $h = 2\pi H/\Lambda$.

The limit of small mean plate separation is very different from the limit of small Nusselt film thickness in the corresponding gravity-driven free-surface film flow over a substrate with the same sinusoidal profile. In the film case, the angle of substrate inclination, α, is important. For sufficiently large inclinations, where $\tan \alpha > a$, all points on the substrate have a downward slope, and therefore as the Nusselt film thickness tends to zero, the result is a complete drainage of the film from the surface of the substrate. On the other hand, when $\tan \alpha < a$, the same limit results in trapped liquid lying stationary in basins formed by the undulations of the substrate. When the Nusselt film thickness is very small but non-zero, eddies are therefore only present at sufficiently small α and sufficiently large a [29].

When the upper boundary is a rigid moving plate, rather than a compliant free-surface, the inclination of the system is irrelevant. The quantity equivalent to the Nusselt film thickness in this case is the clearance, $H - A$, between the upper uniform plate and the tops of the corrugations forming the lower one. The limit $H \to A$ results in a type of lid–driven cavity, and therefore one would expect an eddy to exist even for very small values of a, if $H - A$ is sufficiently small.

3.1   Kinematically induced eddies in Stokes flow

Kinematically induced eddies arise as a result of geometrical constraints, and persist in the limit $\mathrm{Re} \to 0$. In this section, therefore, fluid inertia is neglected, and geometrical effects are explored under Stokes flow conditions. Fig. 3 illustrates the effect of the clearance and waviness on the onset of eddies by plotting the vertical position, C_Y, of the eddy centre as a function of $(H - A)/\Lambda$ for different a. Note that this graph is equivalent to that in Fig. 4

10

in Scholle et al. [24], which considers the corresponding free-surface film flow. Agreement between the finite element and the semi-analytical results is generally good, particularly for small clearances. The deviations for larger clearances are attributable to a decrease in the spatial resolution due to enlargement of the flow region at constant number of modes, N, in the truncated series (14). It is possible to increase the accuracy of the semi-analytical calculations by increasing N, but due to the balance between accuracy and computational effort, this is not done here. The semi-analytical calculations presented are sufficient to corroborate the finite element results, and the latter method is used to produce all subsequent results.

Fig. 3 shows that for large clearances, an eddy centre is only present for sufficiently large a, and that C_Y increases very slowly with increasing clearance. This is similar behaviour to the film case, as one might expect at first glance, given that for large mean gaps/film thicknesses the flow local to the surface of the undulating plate should become insensitive to the exact form of the distant upper boundary. However, there is a difference between the two: in the film case, it is possible to induce a substantial eddy in a previously fully attached flow by increasing the film thickness [24]; this is not possible in the rigid-plate case. This difference between the two flows is due to the different driving forces in the two cases. In the rigid-plate flow, the fluid is driven by the motion of the upper boundary, whose speed, U_0, is independent of the gap between the plates. The free-surface flow, however, is driven by the gravitational body force, resulting in a fluid speed at the free surface proportional to H_f^2 — in fact $U_f = \rho g H_f^2 \sin \alpha / 2\eta$, where H_f is the film thickness and g is the acceleration due to gravity.

Fig. 4 compares the velocity profiles calculated along the vertical centreline of the domain for two different film/gap thicknesses. Consider first the thinner film, where $H_f/A = 7$. This Nusselt film thickness (i.e. that corresponding to a film flowing over a uniform surface) gives rise to a film of mean thickness 7.68 when the same film flows over the wavy plate, as a result of the previously observed film thickening effect of the topography [29]. Hence the rigid-plate flow used to compare with this free-surface flow is that where $H/A = 7.68$. The position of the upper boundary in this case is shown as the lower horizontal dotted line, and corresponds to the free-surface position. The free-surface flow velocity profile is scaled so that $U_f = U_0$ in this case. The difference in the two profiles is clear, with the plate-

11

driven profile showing the expected linearity above the topography, and the gravity-driven profile showing a roughly quadratic form in accordance with Wierschem et al. [30]. When the Nusselt film thickness is doubled (giving a corresponding mean thickness $H/A = 14.698$, shown as the upper dotted line) U_0 remains the same, but U_f is quadrupled, resulting in a much more exaggerated difference in velocity profile. Consequently, increasing the film thickness in the free-surface case tends to increase the shear rate in the upper half of the topography valley, leading to eddy formation, but increasing the gap in the rigid–plate case decreases the shear rate, since U_0 remains fixed.

Returning now to Fig. 3, and considering the change in eddy centre position as H decreases, one can see that for larger values of a, where an eddy already exists, the size of the eddy increases sharply, while for small values of a an eddy is created and rapidly grows as $H \to A$. This is the opposite behaviour to the corresponding free-surface flow, where the eddy disappears as $H_f \to 0$, unless a is sufficiently large, in which case it shrinks in size to a minimum. As $H \to A$, the fact that U_0 is fixed in the rigid-plate flow now acts to increase the shear rate in the valley of the topography and, as explained above, the flow approaches a lid-driven cavity, where an eddy is to be expected.

Note that the levelling off, and subsequent dip in C_Y, as $H \to A$ is a result of the separatrix reaching its maximum extent, as shown in Fig. 5. The limiting value of the eddy depth, D, is $2A$, since then the upper plate makes contact with the lower wavy plate, and becomes the bounding streamline of the eddy enclosed in the resulting closed cavity. However, for small clearances between the plates, the separatrix rises above the tops of the wavy plate, see Fig. 5(a,c). This is a consequence of the difference in shear rate and velocity profile between the shallow inlet and the deep middle of the domain, and the fact that the flux between the upper plate and the separatrix must match that entering (and leaving) the domain. A consequence of the proximity of the upper plate is the change in shape of the separatrix from concave to convex, as seen in Fig. 5(b).

It is evident from Fig. 3 that there is a critical value of the plate clearance which triggers the formation of an eddy in an otherwise fully attached flow, and that this value depends on the waviness of the lower plate. Fig. 6 explores this in more detail via a control space diagram in which the dimensionless clearance, $h - a = 2\pi(H - A)/\Lambda$ is plotted against the waviness, $a = 2\pi A/\Lambda$. The curves show critical combinations of these parameters at

which new eddies are created, with the flow structure in each region of the map indicated by a typical streamline plot. The critical curves were obtained using the shear stress at the lowest point on the lower plate, which varies continuously as the parameters are varied but changes sign when an eddy appears or disappears. Results for the corresponding free-surface film flow based on the experimental results presented by Wierschem et al. [29] in Fig. 8 are shown for comparison purposes. These are given by the two grey-shaded lines indicating the critical Nusselt film thicknesses for the appearance of the first two eddies as a function of the waviness of the substrate. Though the critical values of waviness for large gaps agree with those for thick films in Wierschem et al. [29], the behaviour at small gaps is again opposite to the free-surface case, with the effect of narrowing the gap being to decrease the critical waviness for the appearance of each eddy.

For large gaps, the critical values of waviness, a_{crit}, appear to be equally spaced. This is confirmed in Fig. 7 where the values of a_{crit} are plotted (as black circles) against the number of eddies. The solid line is a linear fit to the data, giving $a_{\mathrm{crit}} = -0.67901 + 1.4653 N_e$ (where N_e is the number of eddies produced), with a correlation coefficient of 0.99992. As a comparison, the corresponding critical values of waviness in the case of free-surface film flow [28], with Nusselt film thickness $h_0 = 10$, are included in Fig. 7. They are seen to be very close to the rigid-plate ones. Note that though the critical curves seem to approach a constant a as $h - a$ increases, they in fact exhibit a maximum a at $h - a \approx 6$ and then show an extremely small decrease in a as $h - a$ increases. This means that the earlier statement that eddies cannot be created by increasing the gap between the plates is not strictly true, since one could in theory fix the value of a very close to but to the left of one of the critical curves, then increase h until the critical curve is crossed. However, the resulting eddy would be so tiny as to be undetectable in practice.

As an aside, it is interesting to explore the relative characteristics of the eddies in the sequence seen at large a, such as that in Fig. 6(*e*). For Stokes flow in a sharp–cornered, straight–sided wedge, driven by an arbitrary distant disturbance, by his well-known analysis Moffatt [31] revealed the existence of an infinite sequence of eddies for wedge angles below a critical value. Adjacent eddies in the sequence were compared in terms of their relative distances from the corner, and their relative 'intensities', as measured by the ratio of local velocity maxima along the wedge centreline. The analysis showed that both of these ratios

are constant for any pair of adjacent eddies in the sequence, and that they depend only on the angle of the corner. In the present problem, the smooth, rounded nature of the bottom boundary results in a finite rather than infinite sequence of eddies, and Table 1 compares adjacent eddies for the conditions in Fig. 6(e). Here n refers to the number of the eddy, with

n	C_Y^n/C_Y^{n+1}	I_n/I_{n+1}	θ_n	R_A^n
1	1.98	362	26.7°	2.03
2	2.57	402	19.1°	2.08
3	—	—	25.1°	2.00

Table 1: Position and intensity ratios for the sequence of eddies shown Fig. 6(e). The ratios between the 3rd and 4th eddies are not given as the 4th eddy is not fully formed in this case.

$n = 1$ being the primary (uppermost) eddy. Following the definitions of Fig. 2, C_Y^n/C_Y^{n+1} is the ratio of the heights of the eddy centres above the lowest point of the valley, while I_n/I_{n+1} gives the relative intensities based on local velocity maxima along the centreline. The angle θ_n represents the angle between the tangents to the upstream and downstream flanks of the valley at a height of C_Y^n, and the quantity R_A^n is an eddy aspect ratio, defined as the ratio of the vertical distance between the eddy's dividing streamlines to the horizontal distance across the valley at height C_Y^n.

As can be seen, neither the position nor the intensity ratio is the same for the two eddy pairs considered, and this is due to the nonlinear form of the boundary. However, the values are consistent with those for a straight-sided wedge, when the variation with wedge angle is considered. See Gaskell et al. [32] for a convenient tabulation of Moffatt's results, and corresponding finite element results for both Stokes and Navier-Stokes flow in a triangular lid-driven cavity. Interestingly, despite the variation in the position and intensity ratios, the aspect ratio of each eddy appears to be essentially constant, at approximately 2.

While the scaling with Λ used in Fig. 6 is useful for revealing the geometric criteria for the appearance of secondary and further eddies, it disguises the behaviour in the small clearance and long wavelength limit. Fig. 8 offers an alternative view by replotting the critical curves using the amplitude, A, as the lengthscale, and plotting the clearance against the wavelength. This illustrates that even for very long wavelengths, there is a critical gap below

which an eddy is present. However, kinematically induced secondary eddies are not possible for large wavelengths, as one would expect. The critical curve for the existence of the primary eddy is reasonably well approximated by $(H - A)/A = 2.3 + 1/[1.03\Lambda/A - 8.25]$, with the asymptotic value of the critical gap therefore being $H_{\mathrm{crit}}/A = 3.3$. The leftmost streamline plots in Fig. 8 also show the expansion and increased curvature of the eddy as the gap is reduced below H_{crit}.

3.2   Inertial effects on kinematically–induced eddies: large gaps

The domain geometry is uniquely specified by three characteristic lengths, namely H, A and Λ, and in this section, H is taken to be larger than both A and Λ. It therefore represents the global scale while A and Λ, which are taken to be of the same order, represent the local scale. This is the configuration considered in the study of the corresponding free-surface film flow [24].

Fig. 9 illustrates the typical effect of increasing Re on the shape of a kinematically induced eddy when H is large. The plot shows the change in eddy depth, the shift in eddy centre position, and the change in shape of the separatrix, when the geometry is fixed and Re increases. For reference, the position of the separatrix and eddy centre at $\mathrm{Re} = 0$ are repeated in the overlaid plots. The effect is qualitatively identical to the free-surface case: the eddy increases in size and becomes asymmetric, with the separatrix higher on the upstream side of the domain [24, 33]. In accordance with this, the eddy centre moves upstream. The curves in Fig. 9 are extremely close to those in Fig. 6 of Scholle et al. [24] but the Reynolds number here is approximately double that in the free-surface case, due to the difference in driving mechanism between the two cases.

In capturing the influence of the wavy substrate geometry on the structure of the flow when $\mathrm{Re} \neq 0$, Scholle et al. [24] used the concept of a 'local Reynolds number', in which the topography wavelength rather than the film thickness is used as the characteristic length. The equivalent quantity in the present rigid-plate problem is

$$\mathrm{Re}_\Lambda = \frac{\rho \Lambda U_0}{2\pi\eta} \, , \tag{17}$$

and this is useful in illustrating how, as Λ decreases, the flow within the shelter of the lower

15

plate becomes essentially decoupled from the inertia–dominated overlying flow. This effect is shown in the bottom graph of Fig. 10, which plots the horizontal shift in the eddy centre position as a function of Re_Λ at a fixed global Reynolds number of $Re = 228$, chosen for comparison with Fig. 8 of Scholle et al. [24].

For small Re_Λ, corresponding to small Λ, the eddy centre lies close to the centreline, and the size of the gap has very little influence on the position. The overlaid streamline plots also show that in this parameter range the eddy structure is symmetrical, despite the global Reynolds number being 228. Hence the flow within the valley is essentially a Stokes flow, and is isolated from the overlying inertial flow. However, at $Re_\Lambda \approx 13$, there is a transition in the behaviour, and for larger Re_Λ the structure becomes markedly asymmetrical, and the size of the gap has a significant influence on the position of the eddy centre. For such conditions the flows within the valley and above the lower plate become fully coupled. Note that in the upper graph, which indicates the variation in the eddy depth, there is no corresponding transition in behaviour, because the size of the eddy is strongly influenced by the waviness in both Stokes and inertial regimes.

As discussed in the previous section, for gaps above the critical value, there is a critical wavelength beyond which kinematically induced eddies no longer appear. Using the relationship $Re_\Lambda = Re \cdot \Lambda/2\pi H$, one can include the critical wavelength in Fig. 10 for each gap, and this is done via the open circles part way along each curve. For conditions to the left of each circle, an eddy would persist if Re were reduced to zero, but for conditions to the right, the eddy would disappear if Re were to be sufficiently reduced. Hence the open circles mark the transition from kinematically to inertially induced eddies. As Re_Λ is further increased, eventually a second critical wavelength is encountered, beyond which the shape of the lower plate is too shallow to sustain an eddy at that particular Re, and the inertially induced eddy therefore disappears. This is indicated by the termination of each curve. Note that for wavelengths (i.e. Re_Λ) beyond the second critical value, it is still possible to generate another eddy by increasing Re sufficiently.

3.3 Inertial effects on kinematically-induced eddies: small gaps

The differences between the present rigid-plate flow and the corresponding free-surface flow for small mean gaps/film thicknesses has already been discussed in the context of Stokes flow, but there is a further difference when inertial effects are of interest. In the free-surface case, it is difficult to increase the Reynolds number substantially when the film is thin, because the characteristic speed of the flow is proportional to the square of the film thickness. In the rigid-plate flow, however, the speed of the moving plate is an independent parameter, allowing a wider range of Re to be realised.

Fig. 11 shows streamline plots which illustrate the change in eddy shape as Re increases, for two different gap sizes. In the upper row, $H/A = 4$, and at first increasing Re has the same effect as described in the last section for large gaps: the separatrix rises on the upstream side to become inclined, and the eddy centre moves upstream (Fig. 11*b*). However, beyond $\mathrm{Re} \approx 50$, the eddy centre moves back towards the centre of the domain, and the separatrix becomes more level as it rises up the downstream flank of the valley (Fig. 11c). For larger Re the eddy centre moves further downstream.

In comparison, when $H/A = 2$, under Stokes conditions the eddy is already closer to the tops of the corrugations forming the lower plate, and in this case increasing Re causes the eddy centre to move directly downstream, resulting in a more exaggerated asymmetry. The effects of Re at different H/A are compared more quantitatively in Fig. 12, which plots the horizontal shift in the eddy centre position. Note here that the sign of ΔX is preserved, with a negative value indicating a shift upstream. For comparison, the ΔX curve from Fig. 9 with $H/A = 14.2$ is included. As can be seen, for intermediate gap sizes, the shift is at first upstream, but after reaching an apparent limiting position, the eddy centre moves back in the downstream direction. Between $H/A = 2$ and $H/A = 3$ there appears to be a critical gap below which the shift in eddy centre position is in the downstream direction only. The downstream shift also appears to have a limiting position, with the eddy centre moving back towards the centre of the domain for very small gaps. This upstream-downstream movement of the eddy centre position is similar to that seen in the classic rectangular lid-driven cavity. In the case of the latter, as Re is increased the eddy centre shifts first in the direction in which the lid is moving, reaches a limiting position and then moves back in the opposite direction

as the flow becomes akin to a solid body rotation; see for example Wright & Gaskell [34].

The most intriguing feature of Fig. 12 is the start of an additional curve near the centre of the plot. This corresponds to a secondary eddy which appears when $H/A = 1.2$. When Re is sufficiently large, the reverse flow along the downstream flank of the valley is sufficiently strong to create an inertially induced secondary eddy. (As Fig. 6 shows, the value of $a = 1.257$ in Fig. 12 is well below the critical value for the appearance of a kinematically induced secondary eddy.) Fig. 13 shows the development of this eddy as Re increases. Since the flow along the lower plate is in this case right to left, the eddy appears on the downstream rather than upstream side of the valley – compare Fig. 13(*c,d*) with the streamline plots in Fig. 10. However, as Re increases, the eddy centre moves upstream, as the left-hand end of its separatrix rises up the upstream flank of the valley.

Clearly inertial effects introduce substantial modifications to the generation and development of eddies, and mapping out the entire parameter space would be a huge undertaking. Rather than attempt to do this, Fig. 14 presents a final observation in the form of the influence of Re on the critical gap H_{crit} for the appearance of an eddy at large wavelengths. Recall that for Stokes flow, Fig. 8 showed that for $H < H_{\mathrm{crit}} \approx 3.3A$ an eddy is always present even for very small waviness. Taking the case $a = \pi/25$ (i.e. $\Lambda/A = 50$) as representative of the long wavelength limit, Fig. 14 shows that H_{crit} increases only slightly for $\mathrm{Re} \lesssim 80$, but increases substantially with Re beyond that range.

4   Conclusions

It has been shown via a systematic theoretical investigation, based on accurate numerical solutions supported by analysis in the Stokes flow regime, that the flow structure associated with plane laminar shear flow over a corrugated plate is influenced by both the geometry (that is, changes to the mean plate separation, in particular the clearance between the moving upper uniform plate and the tops of the corrugations forming the lower one, or the amplitude and wavelength of the corrugations) and the presence of inertia. Revealed also is the subtle interplay that exists between kinematically and inertially induced eddies.

In analysing the effects of geometry on eddy formation, one can separate these into the

18

influence of the waviness of the lower plate and the influence of the mean plate separation. For a large and fixed plate separation, it has been shown under Stokes flow conditions that a sequence of eddies is created as the waviness (i.e. the ratio of amplitude to wavelength) increases. The critical values of waviness at which eddies appear are in very close agreement with those seen in the flow of a correspondingly thick free-surface film over a sinusoidal substrate — as one might expect, assuming that the flow local to the corrugated surface should be insensitive to the exact form of the distant upper boundary.

However, exploration of the influence of the clearance between the plates (and the equivalent Nusselt film thickness for the free-surface case) reveals substantial differences. Starting from a geometry which produces a fully attached flow (i.e. one featuring no eddies), in the free-surface flow it is possible to induce a substantial eddy by increasing the Nusselt film thickness. In the rigid-plate case the opposite is true: an eddy will only be created by sufficiently decreasing the plate clearance. This difference in behaviour is a consequence of the different driving forces involved in the two flows. For the shear-driven rigid-plate flow, the speed of the upper plate is independent of the clearance, while for the gravity-driven free-surface flow, the fluid speed at the free surface is proportional to the square of the film thickness. Hence, velocity profiles along a vertical centreline within the clearance show that the plate-driven system exhibits the expected linearity while the gravity-driven profile for an equivalent Nusselt film thickness is roughly quadratic. If the clearance (film thickness) is doubled the speed of the upper plate (free-surface) is unchanged (quadrupled). Thus, an increase in clearance (Nusselt film thickness) tends to decrease (increase) the shear rate in the upper half of the corrugation, thus retarding (promoting) eddy formation.

As the clearance between the rigid plates tends to zero, the flow approaches that of a lid-driven cavity, in which one would expect to see an eddy. In fact there is a non-zero critical clearance below which a kinematically induced eddy will always be present, even as the waviness of the lower plate tends to zero. As the inertia of the fluid increases, the critical clearance also increases — very slowly for $\mathrm{Re} \lesssim 80$, but then much more rapidly. This larger critical clearance marks the onset of an inertially induced eddy.

For inertial flows with a large plate clearance, a local Reynolds number based on the topography wavelength is useful in understanding how, as the wavelength of the lower plate decreases, the flow within the shelter of the corrugations becomes essentially decoupled

from the inertia-dominated overlying flow. It is found, in the parameter range considered, that for a fixed large global Reynolds number but small local Reynolds number (corresponding to a small corrugation wavelength), the clearance has very little influence on the position and symmetry of an existing eddy; indicating that the flow within the valley region is essentially Stokes-like and isolated from the overlying inertial flow. For larger values of the local Reynolds number an existing eddy becomes markedly more asymmetrical and the clearance has a significant influence with regard to the position of its centre. In such cases the flow within a corrugation and above become fully coupled. Note that since the size of an eddy is influenced by the waviness in both Stokes and non-Stokes flow, there is no corresponding change in behaviour in relation to eddy depth.

Having observed the differences that exist between the rigid-plate and free-surface flows for small clearances and film thicknesses in the context of kinematically induced eddies and Stokes conditions, it is interesting to discover what further differences exist when inertia becomes significant, since in the case of free-surface flow it is difficult to increase the Reynolds number substantially when the film is thin. A key result of the proximity of the driving plate, when the Reynolds number is sufficiently large, is the appearance of an inertially induced secondary eddy at a value of waviness well below the critical value for the appearance of a kinematically induced secondary eddy.

The strength of the inertia present in the laminar shear flow under investigation together with the subtle interplay that exists between kinematically and inertially induced behaviour has a profound influence on the genesis and development of eddies within the flow. To attempt to map out the entire associated parameter space would involve a considerable effort. Nevertheless, the differences in flow structure that can result as described above provide a very useful insight in to the richness of the problem.

Acknowledgement

A   Application of Ritz' direct method for Stokes flow

Transforming the variational principle (10) into the new coordinate system (15) and integrating with respect to R gives

$$I = 2\pi \int_0^1 \ell \, \mathrm{d}Q \tag{18}$$

where

$$
\begin{aligned}
\ell = \;& m \left(\mathrm{i}\xi_n u_m - 2hn u_n u_m - h n v_n v_m \right) I_{1,m+n} \\
& + \frac{h\alpha(Q-1)}{2} \left(4n u_n u_m' + 2n v_n v_m' - \frac{\mathrm{i}}{h}\xi_n u_m' \right) I_{2,m+n} \\
& + \frac{1}{h} \left(J_{1,m+m} - \frac{h\alpha(Q-1)^2}{2} J_{3,m+n} \right) u_n' u_m' \\
& + \frac{1}{h} \left(2J_{1,m+m} - \frac{h\alpha(Q-1)^2}{4} J_{3,m+n} \right) u_n' u_m' \\
& - \mathrm{i}\frac{h\alpha}{h}(Q-1) J_{2,m+n} u_n' v_m' + 2i n v_n u_{-n}' + \frac{1}{h}\xi_n v_{-n}'
\end{aligned}
\tag{19}
$$

with the following abbreviations

$$
\begin{aligned}
I_{1,m} &= \delta_m^0 + \frac{\alpha}{2}\delta_m^{-1} + \frac{\alpha}{2}\delta_m^1 \\
I_{2,m} &= \delta_m^{-1} - \delta_m^1 \\
J_{1,m} &= \frac{\left(-1+\sqrt{1-\alpha^2}\right)^{|n|}}{\alpha^{|n|}\sqrt{1-\alpha^2}} \\
J_{2,m} &= J_{1,m+1} - J_{1,m-1} \\
J_{3,m} &= J_{1,m+2} - 2J_{1,m} + J_{1,m+2} \; .
\end{aligned}
$$

Next, Ritz's direct method is applied by approximating the coefficient functions in (16) as finite linear combinations of $M \in \mathbb{N}$ independent basis functions

$$
u_k(Q) = u_{0,k}(Q) + \sum_{l=1}^{M} u_{l,k}\,\varphi_l(Q) \tag{20}
$$

$$
v_k(Q) = v_{0,k}(Q) + \sum_{l=1}^{M} v_{l,k}\,\varphi_l(Q) \tag{21}
$$

$$
\xi_k(Q) = \sum_{l=1}^{M} \xi_{l,k}\,\phi_l(Q) \tag{22}
$$

with $\varphi_l(0) = \varphi_l(1) = 0$ and arbitrary functions $u_{0,k}$ and $v_{0,k}$ fulfilling the tangential components of the no–slip conditions (7, 8). In the present case the Dirichlet type boundary conditions (7) and (8) results in

$$u_{0,k}(Q) = Q\delta_0^k \qquad v_{0,k}(Q) = 0\,. \qquad (23)$$

As the pressure variation at the boundary is explicit there exists no restriction in the choice of the base functions $\phi_l(Q)$.

For the base functions $\varphi_l(Q)$ use is made of linear combinations of shifted Chebyshev polynomials fulfilling the requirement that $\varphi_k(0) = \varphi_k(1) = 0$, whereas for $\phi_l(Q)$ standard Chebyshev polynomials are used. These allow for fast calculation when computer algebra MAPLE is employeded. Proceeding in this way results in a quadratic expression for the coefficients $u_{l,k}$, $v_{l,k}$ and $p_{l,k}$. Finally, variation with respect to $u_{l,k}$, $v_{l,k}$ and $p_{l,k}$ produces a linear algebraic set of equations for the coefficients which is solved within MATLAB.

References

[1] D. J. Tritton. *Physical Fluid Dynamics, 2nd Edition*. Oxford Science Publications, Clarendon Press, Oxford, 1988.

[2] J. H. Spurk and N. Aksel. *Fluid Mechanics*. Springer, 2008.

[3] B. J. Hamrock. *Fundamentals of Fluid Film Lubrication*. McGraw Hill, 1994.

[4] R. Oliveira. Understanding adhesion: a means for preventing fouling. *Thermal and Fluid Science*, 14:316–322, 1997.

[5] M. Scholle. Hydrodynamical modelling of lubricant friction between rough surfaces. *Tribology International*, 40:1004–1011, 2007.

[6] I. Etsion. State of the art in laser surface texturing. *J. Rheology*, 127:248–253, 2005.

[7] J. J. L. Higdon. Stokes flow in arbitrary two-dimensional domains: shear flow over ridges and cavities. *J. Fluid Mech.*, 159:195–226, 1985.

[8] M. Arghir, N. Roucou, M. Helene, and J. Frene. Theoretical analysis of the incompressible laminar flow in a macro-roughness cell. *J. Tribology*, 125:309–318, 2003.

[9] F. Sahlin, S. B. Glavatskih, T. Almqvist, and R. Larson. Two–dimensional cfd–analysis of micro–patterned surface in hydrodynamic lubrication. *Trans. ASME*, 127:96–102, 2005.

[10] P. H. Gaskell, H. M. Thompson, and M. D. Savage. Stagnation-saddle points and flow patterns in Stokes flow between contra–rotating cylinders. *J. Fluid Mech.*, 370:221–247, 1998.

[11] J. L. Summers, H. M. Thompson, and P. H. Gaskell. Flow structure and transfer jets in a contra–rotating rigid roll coating system. *Theor. Comp. Fluid Dyn.*, 17:189–212, 2004.

[12] M. C. T. Wilson, J. L. Summers, N. Kapur, and P. H. Gaskell. Stirring and transport enhancement in a continuously modulated free–surface flow. *J. Fluid Mech.*, 565:319–351, 2006.

[13] P. H. Gaskell, M. D. Savage, and M. Wilson. Stokes flow in a half–filled annulus between rotating coaxial cylinders. *J. Fluid Mech.*, 337:263–282, 1997.

[14] M. C. T. Wilson, P. H. Gaskell, and M. D. Savage. Nested separatrices in simple shear flow: the effect of localised disturbances on stagnation lines. *Phys. Fluids*, 17:093601, 2005.

[15] A. E. Perry and M. S. Chong. A description of eddying motions and flow patterns using critical–point concepts. *Ann. Rev. Fluid Mech.*, 19:125–155, 1987.

[16] D. J. Jeffrey and J. D. Sherwood. Streamline patterns and eddies in low Reynolds–number flow. *J. Fluid Mech.*, 96:315–334, 1980.

[17] C. Pozrikidis. *Little Book of Streamlines*. Academic Press, San Diego, 1999.

[18] M. Scholle, A. Rund, and N. Aksel. Drag reduction and improvement of material transport in creeping films. *Arch. Appl. Mech.*, 75:93–112, 2006.

[19] M. Scholle, A. Haas, N. Aksel, H. M. Thompson, R. W. Hewson, and P. H. Gaskell. The effect of locally induced flow structure on global heat transfer for plane laminar shear flow. *Int. J. Heat and Fluid Flow*, (in Press), 2009.

[20] C. Pozrikidis. Creeping flow in two–dimensional channels. *J. Fluid Mech.*, 180:495–514, 1987.

[21] M. Scholle. Creeping Couette flow over an undulated plate. *Arch. Appl. Mech.*, 73:823–840, 2004.

[22] A. E. Malevich, V. V. Mityushev, and P. M. Adler. Stokes flow through a channel with wavy walls. *Acta Mech.*, 182:151–182, 2006.

[23] A. E. Malevich, V. V. Mityushev, and P. M. Adler. Couette flow in channels with wavy walls. *Acta Mech.*, 197:247–283, 2008.

[24] M. Scholle, A. Haas, N. Aksel, M. C. T. Wilson, H. M. Thompson, and P. H. Gaskell. Competing geometric and inertial effects on local flow structure in thick gravity-driven fluid films. *Phys. Fluids*, 20:123101, 2008.

[25] P. H. Gaskell, P. K. Jimack, M. Sellier, H. M. Thompson, and M. C. T. Wilson. Gravity–driven flow of continuous thin liquid films on non–porous substrates with topography. *J. Fluid Mech.*, 509:253–280, 2004.

[26] C. B. Millikan. On the steady motion of viscous, incompressible fluids; with particular reference to a variation principle. *Phil. Mag.*, 7:641, 1929.

[27] K.-H. Anthony. Hamilton's action principle and thermodynamics of irreversible processes — a unifying procedure for reversible and irreversible processes. *J. Non–Newtonian Fluid Mech.*, 96:291–339, 2001.

[28] M. Scholle, A. Wierschem, and N. Aksel. Creeping films with vortices over strongly undulated bottoms. *Acta Mech.*, 168:167–193, 2004.

[29] A. Wierschem, M. Scholle, and N. Aksel. Vortices in film flow over strongly undulated bottom profiles at low Reynolds numbers. *Phys. Fluids*, 15:426–435, 2003.

[30] A. Wierschem, M. Scholle, and N. Aksel. Comparison of different theoretical approaches to experiments on film flow down an inclined wavy channel. *Exp. Fluids*, 33:429–442, 2002.

[31] H. K. Moffatt. Viscous and resistive eddies near a sharp corner. *J. Fluid Mech.*, 18:1–18, 1964.

[32] P. H. Gaskell, H. M. Thompson, and M. D. Savage. A finite element analysis of steady viscous flow in triangular cavities. *Proc. Instn. Mech. Engrs. Part C: J. Mech. Eng. Sci.*, 213:263–276, 1999.

[33] A. Wierschem and N. Aksel. Influence of inertia on eddies created in film creeping over strongly undulated substrates. *Phys. Fluids*, 16:4566–4574, 2004.

[34] N. G. Wright and P. H. Gaskell. An efficient multigrid approach to solving highly recirculating flows. *Computers and Fluids*, 24:63–79, 1995.
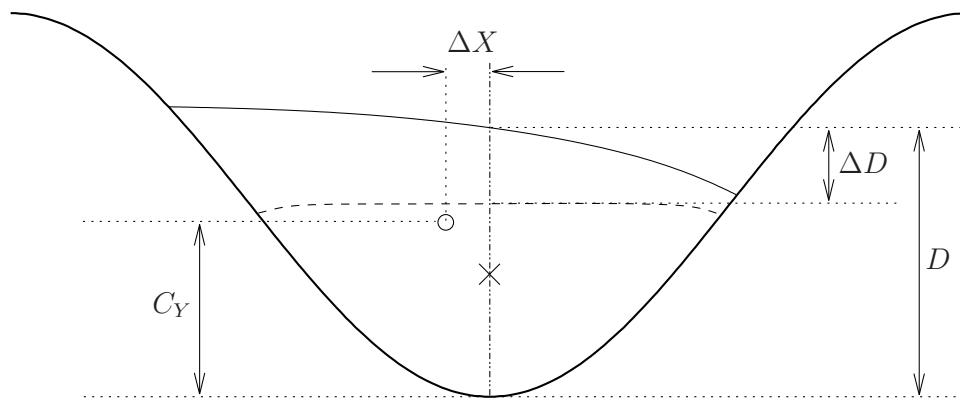
Figure 2: Sketch of the four measurables used to quantify resulting flow behaviour. The solid streamline and open circle mark the separatrix and eddy centre positions under general flow conditions, while the dashed streamline and cross give their corresponding positions for Stokes flow. The quantities ΔX and ΔD therefore refer to the difference in the position of the eddy centre and the eddy depth between the general and Stokes flow cases.
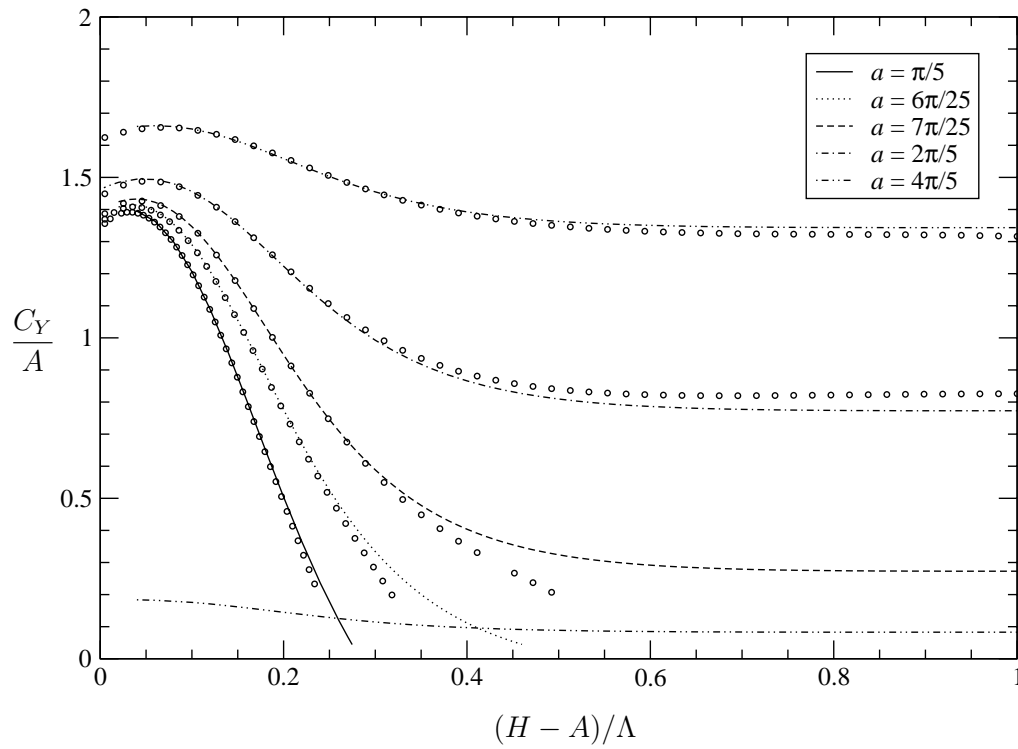
Figure 3: Calculations of the height, C_Y, of the eddy centre above the bottom of the topography, as a function of the gap under Stokes flow conditions. The discrete points give corresponding semi-analytical results with $N = 4$.
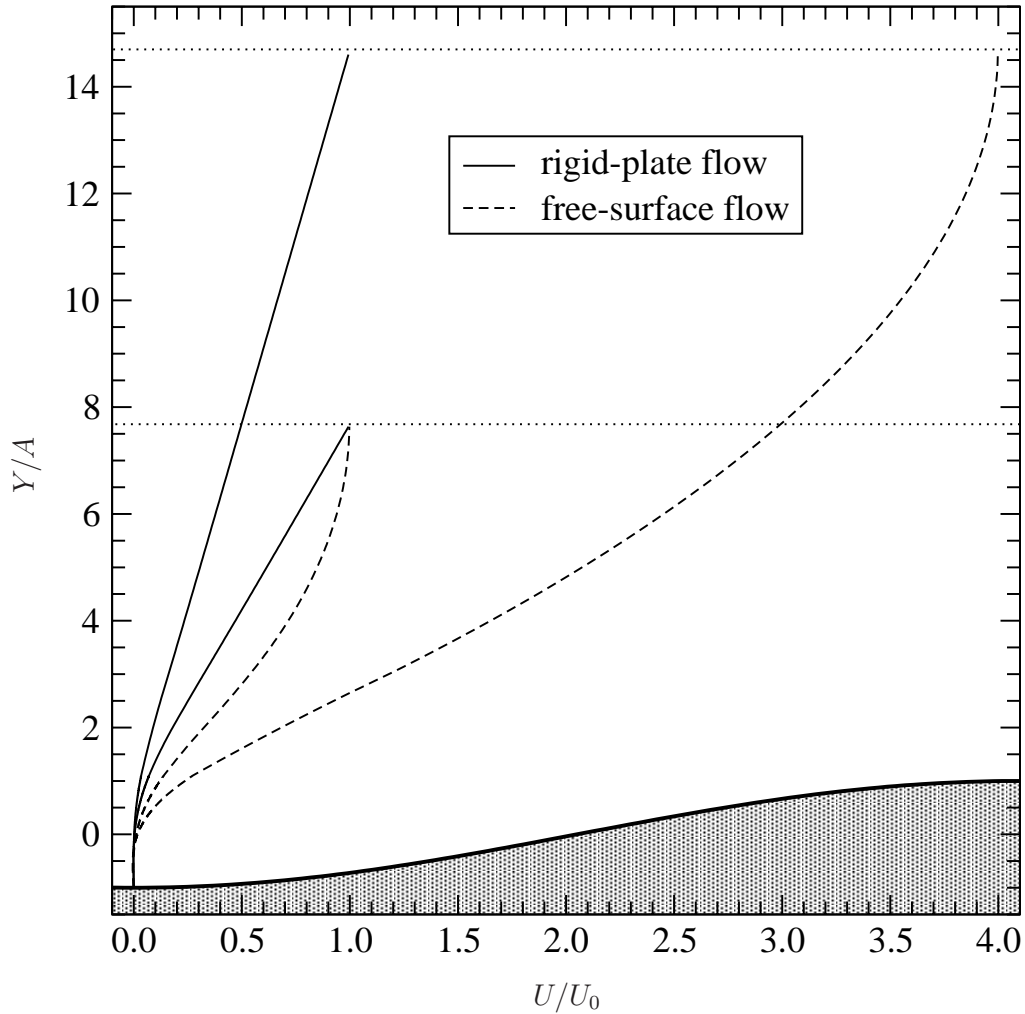
Figure 4: Velocity profiles along the vertical centreline. The curves illustrate the effect of doubling the mean gap (film thickness) on the velocity profiles in the case of rigid plate laminar shear (free-surface film) flow. Lengths are scaled by A. The thick solid line indicates the lower plate surface, and the dotted lines indicate the positions of the upper boundary when $H_f/A = 7$ ($H/A = 7.68$) and $H_f/A = 14$ ($H/A = 14.698$).
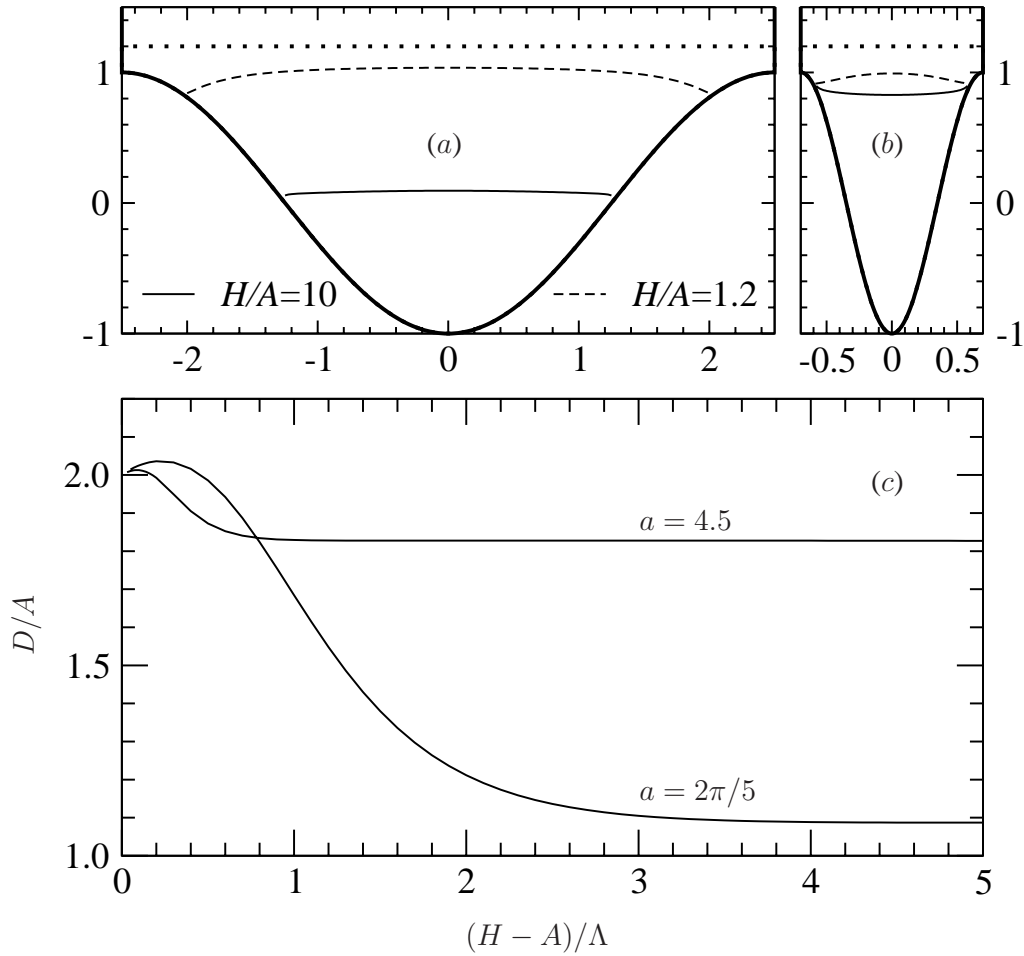
Figure 5: Comparison of the shape and position of the separatrix for different gaps and two different lower plate geometries. In (a) $a = 2\pi/5$, and in (b) $a = 4.5$. Lengths are scaled by A, and the dotted line in each plot shows the position of the upper boundary when $H/A = 1.2$. Graph (c) gives the variation in eddy depth with the clearance.
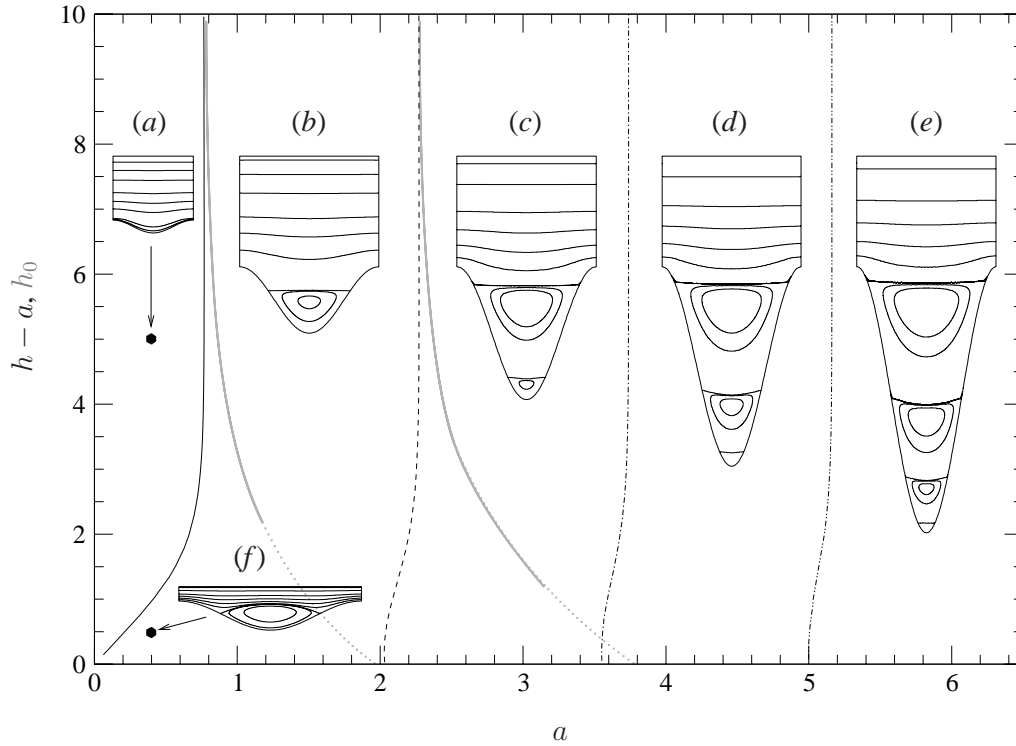
Figure 6: Map of parameter space showing critical combinations of the waviness, a, and clearance, $h - a$, at which the first and subsequent eddies appear. The row of streamline plots (a–e) all have $h - a = 5$, and values of a equal to 0.4, 1.5, 3, 4.5, and 6. Streamline plot (f) corresponds to $h - a = 5$ and $a = 0.4$. For free surface film flow the corresponding critical combinations of the waviness, a, and Nusselt film thickness, h_0, at which the first and the second eddy appear are indicated by the grey–shaded lines.
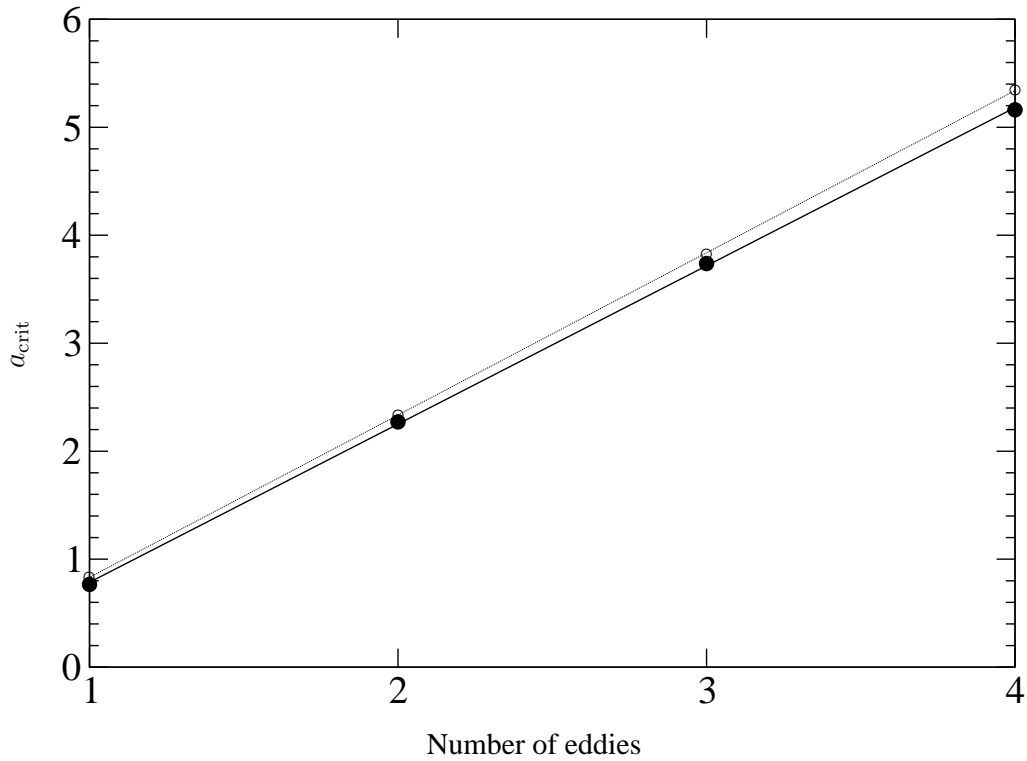
Figure 7: Critical values of waviness, a_{crit}, at which a new eddy appears. The solid circles represent critical values extracted from Fig. 6 at $h - a = 10$. For comparison, the open circles indicate corresponding free-surface film results for a Nusselt film thickness $h_0 = 10$. The solid lines are linear fits to the data.
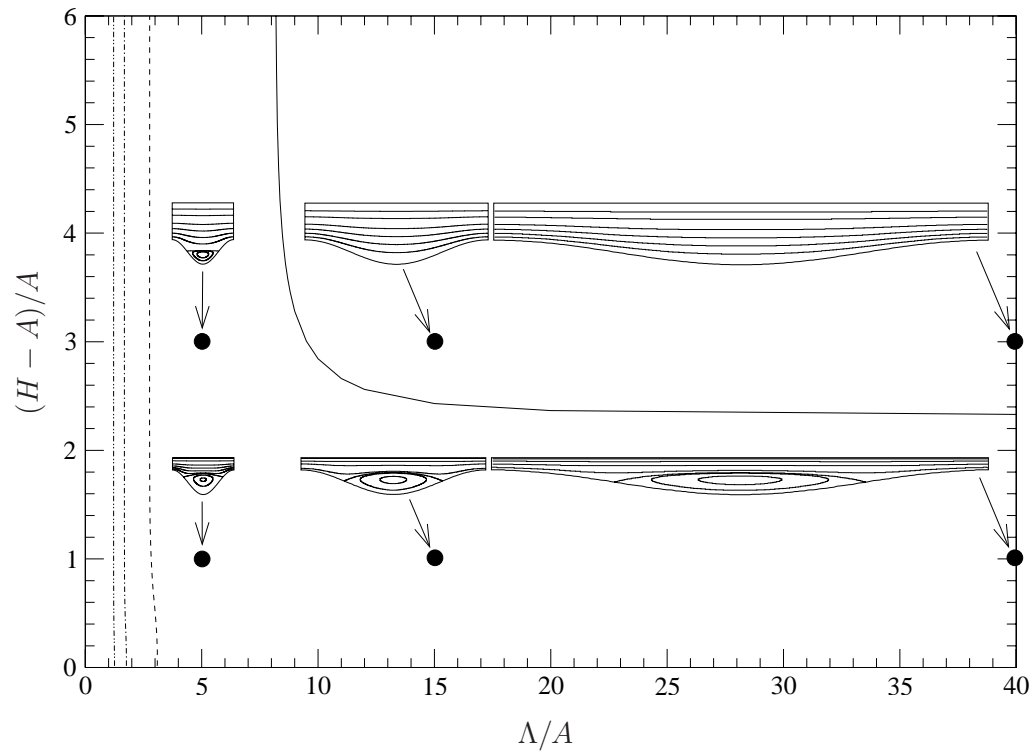
Figure 8: Critical curves of Fig. 6 replotted using the amplitude, A, of the lower plate as the length scale. The streamline plots show the flow structure for the parameter values at the indicated locations.
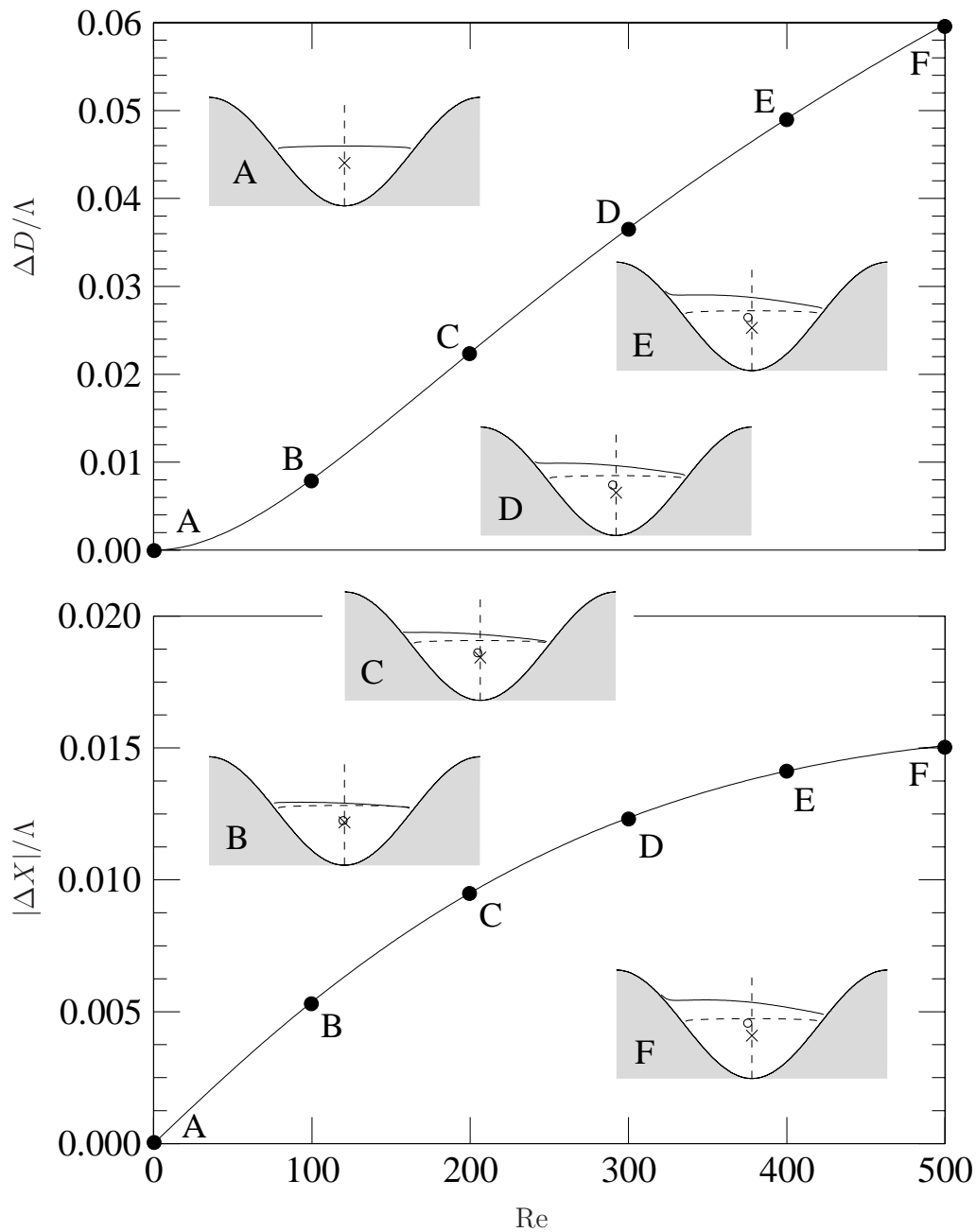
Figure 9: Effect of increasing inertia on the horizontal shift of the eddy centre, $|\Delta X|/\Lambda$ (lower graph), and corresponding change in eddy depth, $\Delta D/\Lambda$ (upper graph), for $H/A = 14.2$ and $a = 2\pi/5$. The overlaid plots A to F show the separatrix and eddy centre position at the values of Re indicated by the corresponding black circles on the graphs. In plots B to F, the separatrix is shown as a solid line, and the eddy centre as an open circle. The Stokes flow separatrix and eddy centre position from A are included in each case as a dashed line and '×' symbol, respectively.
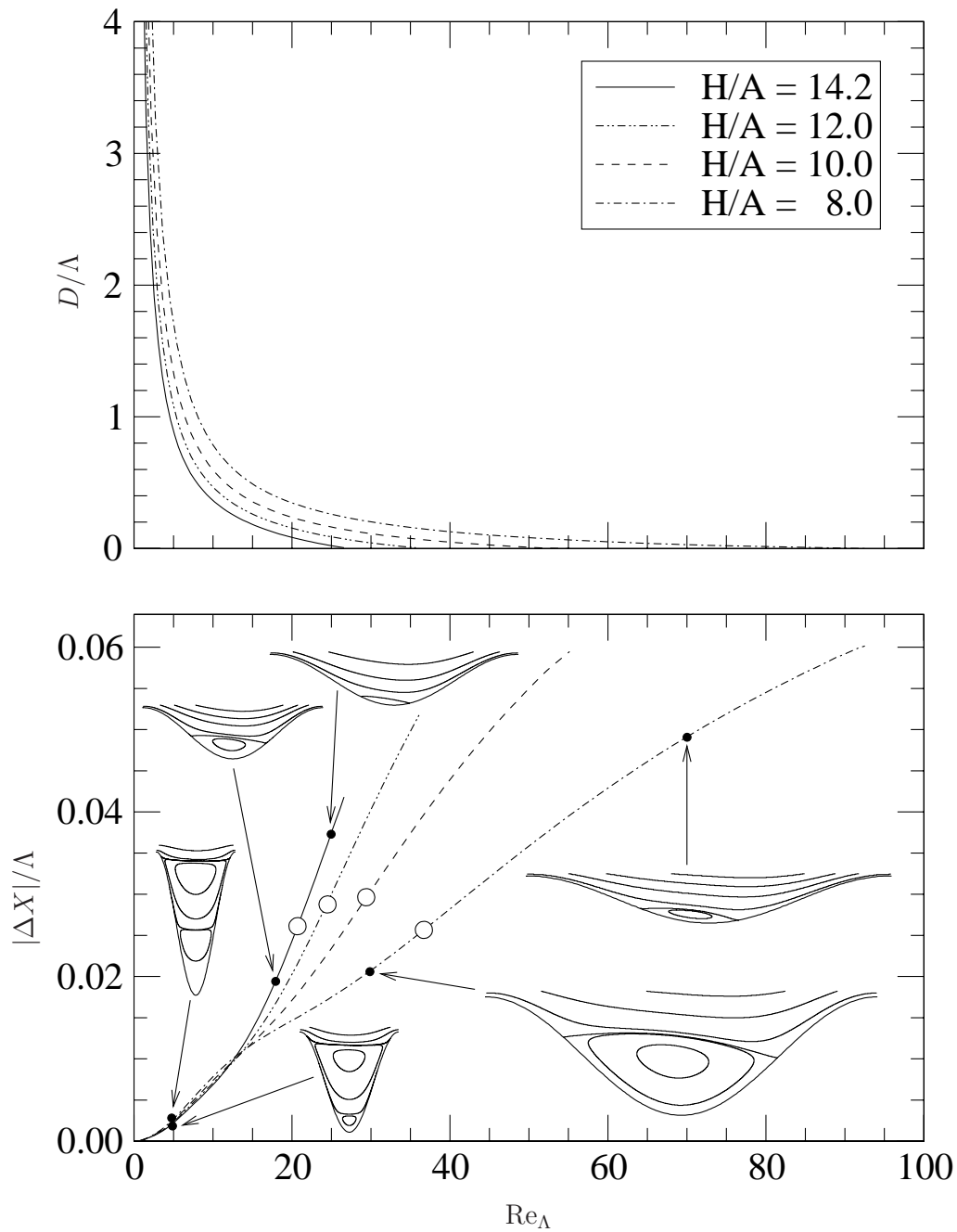
Figure 10: Effect of Re_Λ on the horizontal shift of the eddy centre, $|\Delta X|/\Lambda$, (lower graph) and on eddy depth, D/Λ, (upper graph) for large gaps and $\mathrm{Re} = 228$. The streamline plot inserts illustrate the flow structure for parameter values corresponding to the points shown as the black circles. The open circles mark the transition from a kinematically to inertially induced eddy.
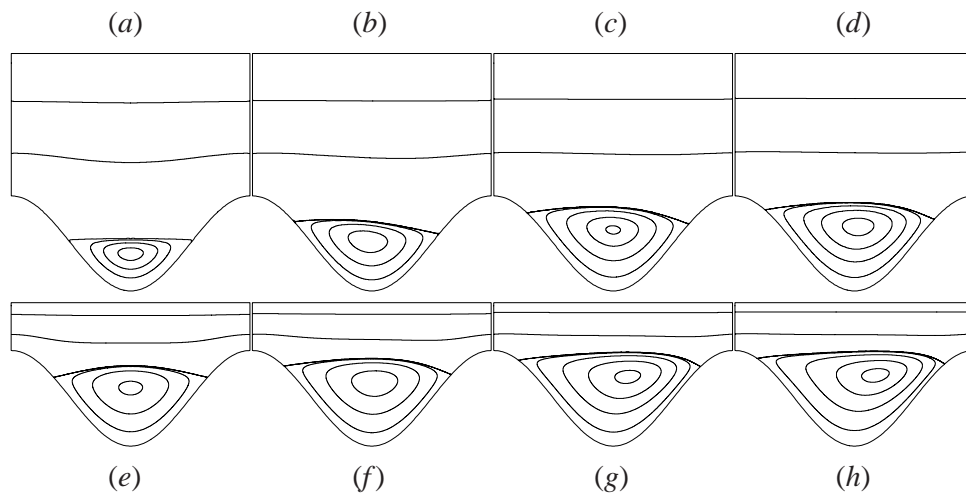
Figure 11: Effect of increasing inertia on eddy shape for $H/A = 4$ (*a-d*) and $H/A = 2$ (*e-h*), with the waviness of the lower plate $a = 2\pi/5 \approx 1.257$. In (*a, e*) $\mathrm{Re} = 0$; in (*b, f*) $\mathrm{Re} = 50$; in (*c, g*) $\mathrm{Re} = 170$; and in (*d, h*) $\mathrm{Re} = 300$.
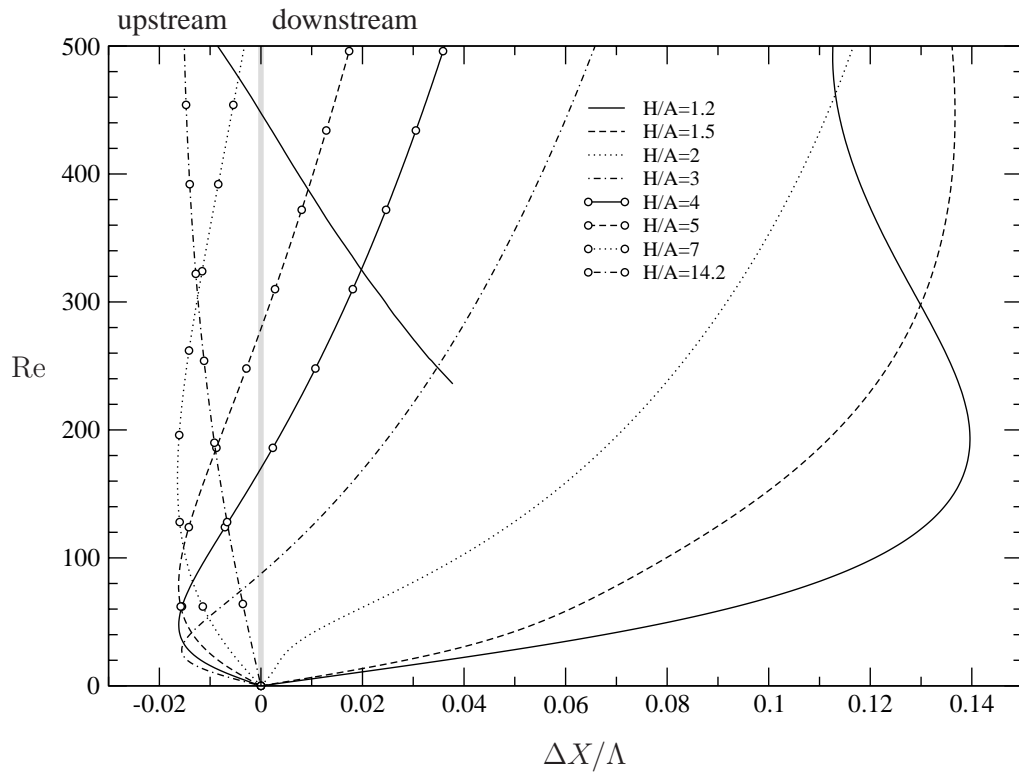
Figure 12: Effect of inertia on the horizontal shift of the eddy centre, $\Delta X/\Lambda$, for $a = 2\pi/5 \approx 1.257$ and a number of different gaps. The solid curve which begins near the centre of the plot corresponds to an inertially induced secondary eddy.
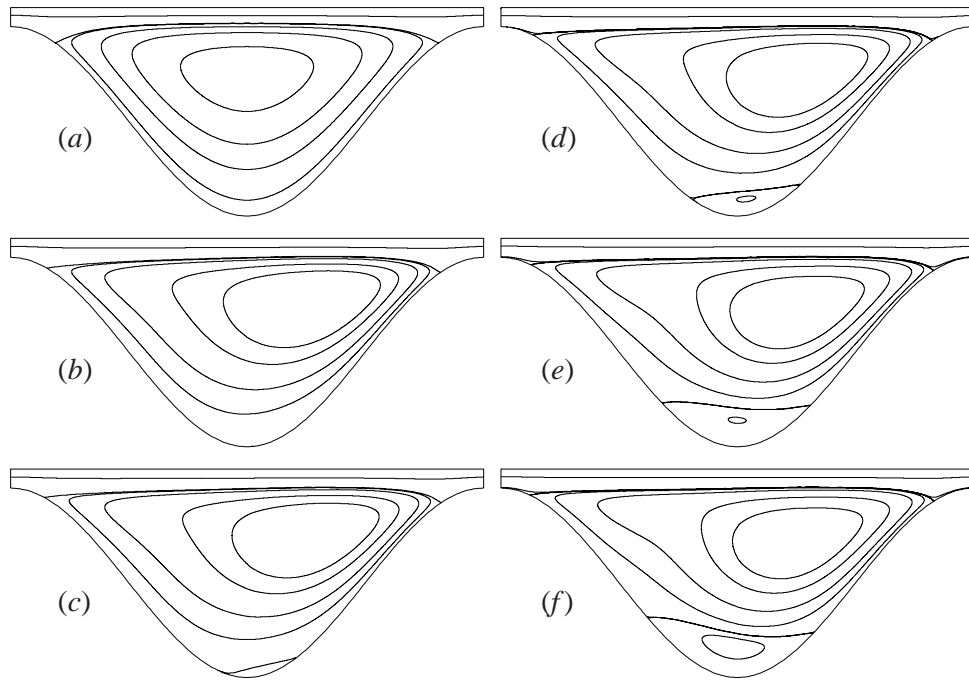
Figure 13: Streamline plots illustrating the generation and development of an inertially induced secondary eddy as Re increases: (*a*) $\mathrm{Re} = 0$; (*b*) $\mathrm{Re} = 200$; (*c*) $\mathrm{Re} = 260$; (*d*) $\mathrm{Re} = 330$; (*e*) $\mathrm{Re} = 450$; (*f*) $\mathrm{Re} = 500$. The geometry is given by $a = 2\pi/5$ and $h = 12\pi/25$, or, equivalently, $H/A = 1.2$ and $\Lambda/A = 5$.
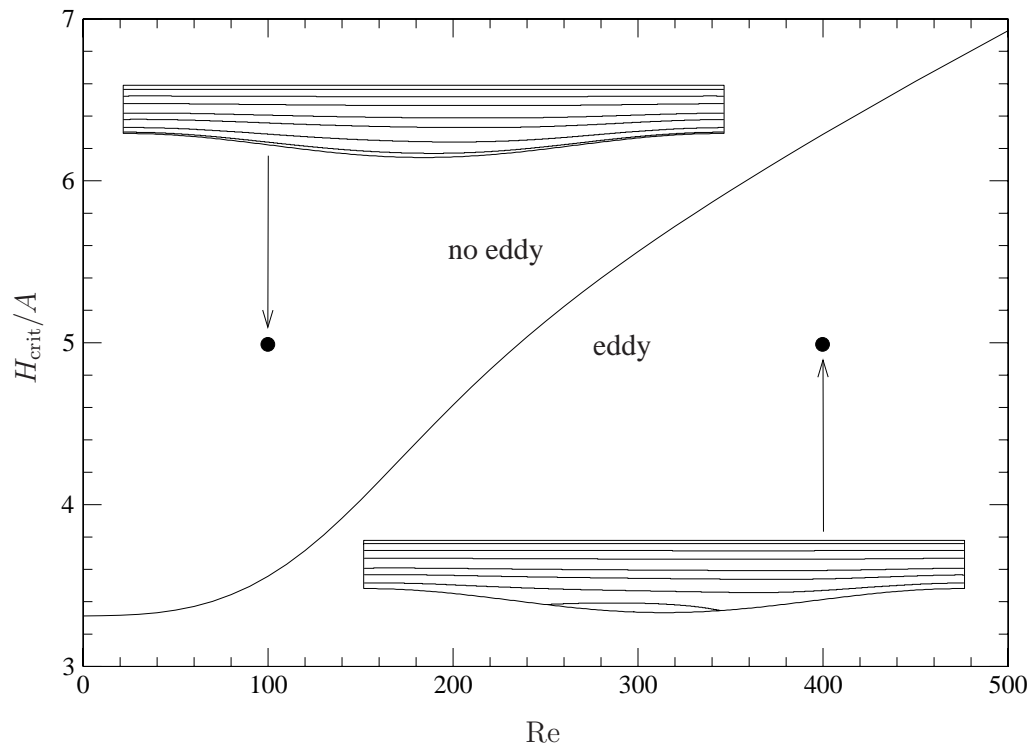
Figure 14: Effect of Reynolds number on the critical gap for the appearance of an eddy at long wavelengths. Here $\Lambda/A = 50$, corresponding to $a = \pi/25 \approx 0.1257$. The streamline plots correspond to the conditions at the indicated black circles.